



HAL
open science

Accounting for sub-wavelength heterogeneities in full waveform inversion based on wavefield gradient measurements

Yann Capdeville, Anthony Sladen

► **To cite this version:**

Yann Capdeville, Anthony Sladen. Accounting for sub-wavelength heterogeneities in full waveform inversion based on wavefield gradient measurements. *Seismica*, 2023, 3 (1), pp.1007. 10.26443/seismica.v3i1.1007 . hal-04360131v2

HAL Id: hal-04360131

<https://hal.science/hal-04360131v2>

Submitted on 23 Aug 2024 (v2), last revised 12 Sep 2024 (v3)

HAL is a multi-disciplinary open access archive for the deposit and dissemination of scientific research documents, whether they are published or not. The documents may come from teaching and research institutions in France or abroad, or from public or private research centers.

L'archive ouverte pluridisciplinaire **HAL**, est destinée au dépôt et à la diffusion de documents scientifiques de niveau recherche, publiés ou non, émanant des établissements d'enseignement et de recherche français ou étrangers, des laboratoires publics ou privés.

DAS sensitivity to heterogeneity scales much smaller than the minimum wavelength

Yann Capdeville *¹, Anthony Sladen ²

¹Nantes Université, Univ Angers, Le Mans Université, CNRS, Laboratoire de Planétologie et Géosciences, LPG UMR 6112, 44000 Nantes, France,

²Université Côte d'Azur, CNRS, Observatoire de la Côte d'Azur, IRD, Géoazur, Sophia Antipolis, 06560, Valbonne, France

Author contributions: *Conceptualization, Methodology*: Yann Capdeville.

Abstract Distributed Acoustic Sensing (DAS) is a photonic technology allowing to convert fiber-optics into long (tens of kilometers) and with high linear density (every few meters) arrays of seismo-acoustic sensors which are basically measuring the strain of the cable all along the cable. The potential of such a distributed measurement is very important and has triggered strong attention in the seismology community for a wide range of applications. In this work, we focus on the interaction of such measurements with heterogeneities of scale much smaller than the wavefield minimum wavelength. With a straightforward 2-D numerical modeling, we first show that the effect of such small-scale heterogeneities, when located in the vicinity of the instruments, is very different depending on whether we measure particle velocity or strain rate. Specifically, when measuring particle velocity, the effects of small nearby heterogeneities are small whereas, when measuring strain rate, the effects are large. We then provide a physical explanation of these observations based on the homogenization method showing that indeed, the strain sensitivity to nearby heterogeneities is strong, which is not the case for more traditional velocity measurements. This effect appears as a coupling of the strain components to the DAS measurement. Such effects can be seen as a curse or an advantage depending on the applications.

Non-technical summary Fiber optics are commonly used in telecommunications, typically for high-speed internet. Recently, it has been shown that together with a photonic device called Distributed Acoustic Sensing (DAS), they can also be used to record ground deformation as a function of time, something close to what a seismometer does. Such an application of fiber optics has triggered a lot of attention among seismologists because it is an affordable and simple way to have many seismic sensors distributed along existing or new fibers. Nevertheless, DAS records the deformation of the ground whereas seismometers typically record ground velocity or acceleration. This subtle difference makes DAS very sensitive to details of the grounds nearby the fiber optics. This can be a great advantage to detect or analyze heterogeneities that are close to the DAS fiber. Nevertheless, it can be also a serious issue as signals from the nearby heterogeneities can hide signals coming from far distances, typically the one used to detect earthquakes for example. The objective of this work is to understand this special sensitivity to small ground heterogeneities near the fiber-optic cables and potentially correct it or use it.

1 Introduction

Distributed Acoustic Sensing (DAS) is a photonic technology allowing the conversion of fiber-optics into long (> 100 km) with high linear density (every few meters) arrays of seismo-acoustic sensors. Applications were first developed in the fields of exploration and reservoir monitoring (e.g., Mateeva et al., 2012; Daley et al., 2013) and relied on both dedicated fiber-optic (FO) cables and medium coupling set up to improve the quality of the recordings. The attachment of the Fiber Optic (FO) cable to both its cable jacket and the ground is known to strongly affect DAS measurements (e.g., Papp et al., 2016). In 2017, Lindsey et al. demonstrated that DAS acquisitions could be performed on pre-existing telecom FO cables and provide valuable earthquake signals, matching the sensitivity of standard seismome-

ters down to frequencies of a few tenths of Hertz (Hz). Typically, those telecom cables are simply pulled in underground conduits, and the FO is decoupled from the outer jacket (so-called loose fibers), two setup conditions that should not favor good-quality recording. Yet, experience shows that gravity and friction, while not optimal, are usually sufficient to reach the data minimum quality required for many applications. The potential of DAS to leverage existing FO cables was later expanded to seafloor telecom cables (e.g., Lindsey et al., 2019; Sladen et al., 2019; Williams et al., 2019): in this case, the cables have several additional protective and rigid layers to prevent damage from fishing activities or seafloor abrasion. The possibility of leveraging the immense and global network of telecom cables, both on land and at sea, is decisive in the current development of the technology to monitor diverse signals such as those from cars, boats, insects, marine mam-

Production Editor:
Gareth Funning
Handling Editor:
Stephen Hicks
Copy & Layout Editor:
Jack B. Muir

Received:
May 19, 2023
Accepted:
December 20, 2023
Published:
January 25, 2024

*Corresponding author: yann.capdeville@univ-nantes.fr

mals, seafloor currents or sea-ice formation (van den Ende et al., 2021; Rivet et al., 2021; Wang et al., 2021; Bouffaut et al., 2022; Mata Flores et al., 2022; Baker and Abbott, 2022). But, piggybacking on existing cables implies little to no control over how the fiber is deployed and couples to the medium. While DAS-related studies often assume uniform coupling (e.g., Mateeva et al., 2014; Kuvshinov, 2016), in practice DAS data can show great variability in sensitivity and fidelity between neighboring sensors, with a signal-to-noise ratio (SNR) often lower than state-of-the-art seismic sensors (e.g., Mateeva et al., 2014; Wang et al., 2018). Even experiments with dedicated and optimized cable setups can show many localized signatures, such as amplitude discontinuities or phase jumps, which are difficult to interpret and hinder our ability to fully assess the sensors' response. A common difficulty in understanding localized signatures is the inability to reach the cable sections of interest and diagnose them, for instance when the cable is in the casing of a borehole, in underground conduits, or on the seafloor. Another major difficulty can stem from the nature of the DAS measurement itself: because DAS measures the local strain or strain rate, the measurements are more sensitive to local coupling variations, local changes in topography, or elastic constants in the medium than if it were particle displacement or velocity point measurements, like with seismometers (e.g., Harrison, 1976; Gombert and Agnew, 1996; Berger and Beaumont, 1976). This difference in sensitivity has been explored theoretically, experimentally, and numerically by van Driel et al. (2012) and Singh et al. (2020). Here, following these two works, we focus on the impact of heterogeneities smaller than the minimum wavelength, illustrating their impact on the DAS data through numerical simulations and theoretical considerations.

The paper is organized as follows: we first recall the principles of DAS measurements and present examples of potential interaction between seismic waves and scales much smaller than the minimum wavelength. We then present a numerical experiment involving small heterogeneities showing similar spatial variations. Finally, we interpret these effects in light of the homogenization theory before discussing the results and concluding.

2 Principles of DAS measurements

To understand how small-scale heterogeneities might influence the measurements, it is important to recall what DAS interrogators are effectively measuring. The basic principle is to track changes in the optical path along the FO by analyzing Rayleigh back-scattered light (Nakazawa, 1983). Rayleigh scattering is caused by the interaction between the laser light and molecular defects in the silica glass which are much smaller than the injected wavelength. The distributed nature of DAS measurements is made possible by the omnipresence of these defects in the FO waveguide and the ability to locate isolated changes along the fiber path with the two-way travel time of light. For FO aligned with the x -axis, thanks to the elastic nature of the FO for small deforma-

tion, it is possible to relate optical phase variations $\Delta\Phi$ over a segment L_G to its strain ϵ^{DAS} (e.g., Hartog, 2017):

$$\epsilon^{\text{DAS}}(\mathbf{x}, t) = \frac{\lambda}{4\pi n \xi L_G} \Delta\Phi(L_G; \mathbf{x}, t), \quad (1)$$

where λ is the laser wavelength used to probe a FO of optical index n . ξ is assumed to be constant, typically 0.79 in single-mode fiber, and acknowledges that straining the fiber also implies a proportional change in its refractive index. ϵ^{DAS} is often approximated as being equal to the local longitudinal strain, but the recorded signal can involve some additional terms. The ability to track small phase changes $\Delta\Phi$ is related to the wavelength of the laser source, which is very small (typically 1550 nm, the telecom standard which minimizes optical attenuation), allowing some interrogators to go beyond $10^{-12}\epsilon/\sqrt{\text{Hz}}$ sensitivity over 10 km (e.g. Ogden et al., 2021). The sampling frequency is limited by the need to recover the back-scattered light of a laser pulse before launching a new one and the need to stack measurements to reach a reasonable SNR.

Depending on if the phase difference is measured relative to a reference one or the previous one, DAS systems will provide strain or strain-rate data respectively. Thermal fluctuations can also cause phase changes but are assumed negligible when looking at periods shorter than a few minutes (e.g. Bakku, 2015), which is the case for most DAS applications. The width of the laser pulse will control the minimum distance over which the phase can be independently averaged, generally a few meters. Smaller pulses are possible and provide higher resolution, but are usually not favored because of the lower SNR. Thus, the receiver spacing called the gauge length (L_G), cannot be smaller than the pulse width which is predefined in any acquisition. Standard DAS acquisitions use a gauge length of around 10-20 meters which offers a good trade-off between the spatial resolution and the SNR in seismic applications (Dean et al., 2017).

In its simplified form, DAS measurements can be described as the difference in the horizontal velocity at the endpoints of gauge length segments. To go from the actual strain rate $\dot{\epsilon}$ (the time derivative of ϵ) along the FO cable to the corresponding DAS measurement $\dot{\epsilon}^{\text{DAS}}$, one has to take into account the effect of the gauge length L_G . For a FO cable aligned with the x -axis and assuming a homogeneous medium it takes the form (Wang et al., 2018):

$$\begin{aligned} \dot{\epsilon}^{\text{DAS}}(x, t) &= \frac{1}{L_G} \int_x^{x+L_G} \dot{\epsilon}(l) dl \\ &= \frac{1}{L_G} \int_x^{x+L_G} \frac{\partial}{\partial t} \frac{\partial u}{\partial l} dl \\ &= \frac{v_x(x+L_G, t) - v_x(x, t)}{L_G}, \end{aligned} \quad (2)$$

where l is a position along the fiber and v_x is the x -component of the particle velocity. For most applications, the gauge length L_G mainly behaves like a moving average in the spatial domain. But for high-frequency applications, the seismic wavelength will become comparable to the gauge length which may also cause aliasing and amplitude distortions (Lomnitz, 1997; Dean

et al., 2017; Hubbard et al., 2022). Another smoothing effect is because the Rayleigh back-scattering is not monitored by the DAS interrogator at single points along the FO cable, but over a length defined by the pulse width (Dean et al., 2016). The pulse width is typically 5-10 times smaller than the gauge length meaning that its smoothing effect is more limited than for the gauge length and has an effect only at higher wavenumbers. In the following, we assume the effect of the pulse width can be neglected.

3 DAS observation small-scale anomalies

To illustrate the variability commonly observed in DAS acquisitions, we plot the record of a local magnitude 2.7 earthquake aftershock (Fig. 1) acquired on a telecom cable in the southwest of France (Lon: 4.65° , Lat: 44.55° at 22:14 UTC French national seismic network RéNaSS). This data sample is part of a campaign organized to record the seismicity following the damaging M_W 4.9 earthquake of November 11th, 2019 (Cornou et al., 2021). The DAS system is an AR-1 first-generation system from the Febus Optics company, configured to record strain rate at 400 Hz with a gauge length of 9.6 m and spatial sampling of 3.2 m. The FO cable mainly follows countryside roads to form a V-shape network of 4375 sensors over 14 km: the north arm of the cable measures approximately 8 kilometers in length, whereas the east-west arm is approximately 6 kilometers in length. In Fig. 1b, we can distinctly identify the P and S phase arrivals and propagation across the array. The amplitude of the wavefield changes significantly at the scale of several to hundreds of channels (tens to thousands of meters). Most of that variability should be related to changes in the coupling conditions of the fiber. There might be also an influence of local changes in the fiber orientation relative to the wavefield, to which the DAS response is strongly sensitive (Bakku, 2015; Martin, 2018). Many of the sections with large amplitudes have long-lasting signals (several seconds) with significantly slower phase velocities: these correspond to diffracted surface waves caused by the presence of slower near-surface material, and possibly low-velocity fracture zones further trapping seismic energy (Cheng et al., 2021; Lior et al., 2022). We also observe many signals that are difficult to associate with a propagating seismic wave. An example of such signals is highlighted by a white box in Fig. 1(b) and by a cyan box in Fig. 1(c). They have the following characteristics:

1. they display rapid spatial changes present in most frequency bands. Their spatial width (apparent wavelength) is mostly independent of the frequency band, (but their wave shape details can change);
2. they appear for all/most times for a given position along the fiber.

The first characteristic is not compatible with a wave dispersion relation. Indeed, following the dispersion relation, a wavefield wavelength is expected to be longer

and longer for lower and lower frequencies. The second characteristic is, in general, not compatible with wave propagation, (unless we have a plane wave propagating perpendicular to the FO). A signal that displays both characteristics is unlikely to be a classical propagating wave signal and is referred to as an “anomaly” in the rest of the paper.

To explore the small-scale anomalies, we band-pass filter this dataset between a low-frequency cutoff of 0.06 Hz and several high-frequency cutoffs of 3, 6, 15, or 25 Hz. For each filtered version of the dataset, we then extract the signal at four different times for the same 900 sensors (materialized by horizontal black lines in Fig. 1(b)). At each time, it is possible to observe a signal related to the main seismic phases: this signal is most visible for the larger bandpass filter (0.06-25Hz) but tends to attenuate as we decrease the high-frequency cutoff (15, 6, 3Hz). For instance, this filtering effect is visible in the first and third profiles which intersect the P and S wavefronts, shown by red and blue boxes in Fig. 1 respectively. One particular example is highlighted with a magenta box in Fig. 1(c) for the S-wave. This is not obvious because the signal is noisy, its amplitude decay for lower frequencies and the signal is dominated by anomalies, but it can nevertheless be seen that the apparent wavelength is larger for lower frequencies. This is the behavior we expect from the dispersion relation: the wavelength should change with the frequency band such that larger wavelengths should be observed for lower frequencies. Yet, we see that some localized perturbations, over one or a few channels, don't seem to be affected by the level of filtering, and they appear for all times (see the white and cyan boxes in Fig. 1(b) and Fig. 1(c) respectively).

These localized anomalies could be due to the DAS acquisition or a change in the nearby environment of the fiber such as variations in the coupling conditions, or heterogeneities in the medium. Two well-known sources of anomalies inherent to DAS technology are phase unwrapping errors (e.g. something directly touching the OF and causing a sudden large strain) and laser frequency drifts (e.g. if the laser of the DAS is affected by external vibrations). But both effects are expected to generate anomalies at specific times over many or all channels when our observations show the opposite. DAS acquisition can also be affected by fading, which is the destructive interference of the back-scattered electric fields over the gauge length. However, fading should manifest as low SNR channels rather than anomalies standing out of the noise. So, are these anomalies related to the environment of the fiber? Concluding on this question would require a detailed inspection and testing of each of the corresponding fiber sections, which is beyond the scope of this paper. But in the following sections, we explain how mechanical property heterogeneities at scales comparable to the gauge length, and in the close environment of the fiber, are a possible explanation. Please note that the following numerical experiments do not constitute modeling of the actual data setting presented here; instead, they represent a simplified toy model that illustrates the effects we intend to emphasize.

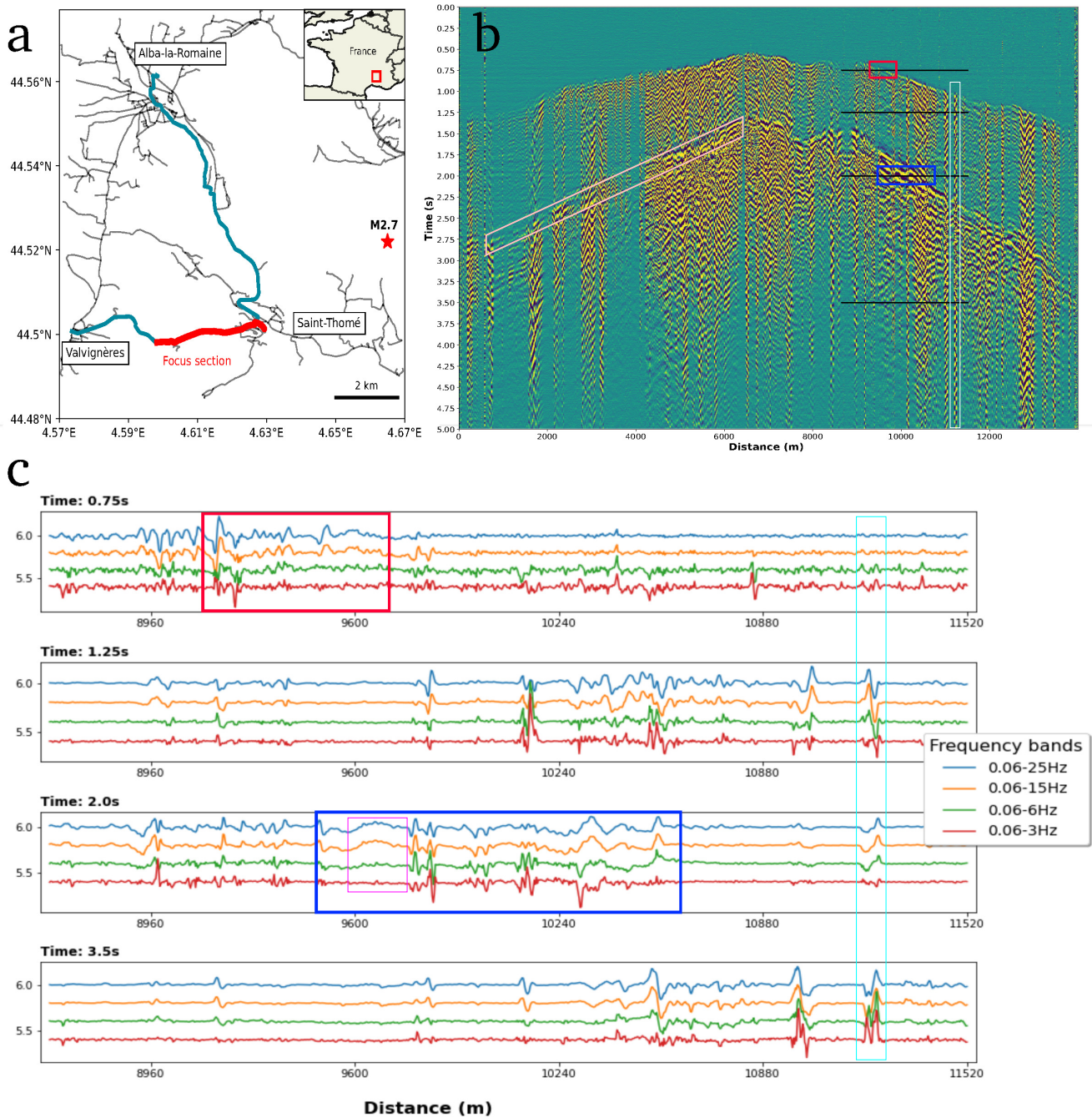


Figure 1 (a) Map of the telecom FO cable monitored with DAS. (b) DAS waterfall plot of an $M2.7$ aftershock recorded on November 23, 2019, showing the P and S wave arrivals (c) DAS data extracted from the four black profiles of the top figure after the DAS data had been filtered in time over different frequency bands and represented by different colors. The red and blue boxes highlight the P and S wave arrivals. In (b), the pink box focuses on one side of the S-wave front arrival. The white box highlights one example of the many “anomalies” mentioned in the text. In (c), the red and blue boxes correspond to the red and blue boxes in (b). The magenta box highlights the S-wave arrival for that time, and the cyan box highlights the same “anomaly” example as the one highlighted in white in (b). Please note that, in the cyan box, the anomaly is not visible for $t = 0.75s$. This is because the seismic wave hasn’t reached the FO cable yet.

4 Numerical Observations

In this section, we set up a simple numerical experiment showing interactions of DAS measurements with heterogeneities of size much smaller than the wavefield minimum wavelength λ_{\min} . In the following, “small-scale” always means small relative to λ_{\min} . We consider waves in a 2-D elastic domain Ω with absorbing boundary conditions on its boundary $\partial\Omega$, such that Ω can be considered as an infinite plate (no waves are bouncing on $\partial\Omega$). In Ω , we use a (x, z) Cartesian coordinate system of unit vectors \hat{x} for the x -axis and \hat{z} for the z -axis. Please note that the z -axis doesn't refer to a depth in the present work. In Ω , the particle displacement vector $\mathbf{u}(\mathbf{x}, t)$ is driven by the elastic wave equation,

$$\rho \partial_{tt} \mathbf{u} - \nabla \cdot \boldsymbol{\sigma} = \mathbf{f}, \quad (3)$$

$$\boldsymbol{\sigma} = \mathbf{c} : \boldsymbol{\epsilon}(\mathbf{u}), \quad (4)$$

where $\epsilon_{ij}(\mathbf{u}) = \frac{1}{2}(\partial_i u_j + \partial_j u_i)$ is the strain operator, $(i, j) \in \{x, z\}^2$, $\rho(\mathbf{x})$ is the density, $\mathbf{c}(\mathbf{x})$ the elastic tensor, $\boldsymbol{\sigma}(\mathbf{x}, t)$ the stress tensor and \mathbf{f} the source term and $\mathbf{x} = (x, z)$ the position vector in Ω . We use a point source such that

$$\mathbf{f}(\mathbf{x}, t) = -\mathbf{M} \cdot \nabla \delta(\mathbf{x} - \mathbf{x}_0) g(t), \quad (5)$$

where \mathbf{M} the moment tensor, x_0 the source location and $g(t)$ the source time wavelet. We solve (3-4) using the Spectral Element Method (SEM) (Komatitsch and Vilotte, 1998; Chaljub et al., 2007) with Perfectly Matched Layer (PML) absorbing boundaries on $\partial\Omega$ (Festa and Vilotte, 2005).

In the following, for the sake of simplicity, we consider FO cables deployed along the x -axis with a z -axis constant position $z = z_c$. To mimic the DAS measurements, we record the x components of the velocity $v_x(\mathbf{x}, t)$ at discrete locations L_G meters apart along each cable. This discrete set of the recording locations along the DAS cable x_i leads to a set of time series $v_x(x_i, z_c, t)$. The DAS measurement can be then computed as:

$$\begin{aligned} \dot{\epsilon}^{\text{DAS}}(x_i, t) &= \Delta_x v_x(x_i, z_c, t) \\ &= \frac{v_x(x_{i+1}, z_c, t) - v_x(x_i, z_c, t)}{L_G}, \end{aligned} \quad (6)$$

The DAS measurement corresponds to a finite difference in the cable direction, here noted Δ_x , applied to the particle velocity along the cable. In general, it is different from the x -partial derivative ∂_x . Δ_x can be a good approximation of ∂_x only in some circumstances that will be discussed later on.

In the next two sections, we present a simple 2-D numerical experiment. The chosen configuration is not intended to be fully realistic. In particular, it is not intended to model the particular data setting presented in Section 3. Rather, it is designed to highlight the fundamental difference between DAS measurements and classical velocity measurements when it comes to their interactions with nearby small-scale heterogeneities. The experience of most seismologists is based on classical ground displacement measurements (from seismometers to accelerometers) for which small-scale heterogeneities near the receivers have little effect. The

strong effect of such heterogeneities on DAS measurements, that we are about to show, might be non-intuitive for many.

The geometrical setting of the numerical experiment is shown in Fig. 2. Ω is a $20 \times 40 \text{ km}^2$ rectangle of slow material ($V_P = 0.8 \text{ km/s}$, $V_S = 0.5 \text{ km/s}$, $\rho = 900 \text{ kg/m}^3$), in which are embedded stiff small heterogeneities that we name “stones” ($V_P = 4.4 \text{ km/s}$, $V_S = 2.7 \text{ km/s}$, $\rho = 2400 \text{ kg/m}^3$). Ω can be seen as an horizontal plane, a kind of a top view of a real DAS experiment. Nevertheless, it is only a partly relevant analogy of the reality as in such a case, the free surface is not present (see the discussion section for more about the relevance of the modeling). Nonetheless, this simplified model is adequate to illustrate our main point: the impact of small-scale heterogeneities on DAS measurements. Specifically, it effectively demonstrates the distinction between displacement and strain measurements associated with DAS when heterogeneities of significant mechanical property contrast are in a close proximity to the FO cable. 50 square shape stones of edge size in the $[20 \text{ m}, 30 \text{ m}]$ range, with arbitrary orientation are generated randomly. The stones' locations are also generated randomly but are limited to a small region around the cables to minimize the wavefield complexity. In this numerical experiment, we simulate the presence of two FO. To mimic them, two parallel 12 km long measurement lines are defined in $z_c = 30.18 \text{ km}$ (FO1) and $z_c = 30.08 \text{ km}$ (FO2), both parallel to the x -axis and starting at $x = 4 \text{ km}$. In both cases, we use a sampling rate $L_G = 15 \text{ m}$ between each displacement measurement along the lines. The line locations are chosen such that FO1 is directly in contact with 7 stones and FO2 with none (see Fig. 2. Please note that only 6 of the 7 stones in contact with FO1 are visible in the zoom of Fig. 2(b)).

The source is located 20 km away from the cables, in the lower right part of Ω . It is an explosion (\mathbf{M} is the identity matrix) and g is Ricker (second derivative of a Gaussian) with a central frequency $f_0 = 0.85 \text{ Hz}$, leading to maximum frequency $f_{\max} \simeq 2.5 \text{ Hz}$ (see Fig. 3), such that the background minimum wavelength $\lambda_{\min} \simeq 220 \text{ m}$. λ_{\min} is therefore much larger than the size of the edge of the stones (30m). The central time of the Ricker is $t_0 = 2 \text{ s}$.

To obtain accurate modeling, it is necessary to honor all the strong contrasts of mechanical property discontinuities between the background and the stone materials with element mesh boundaries. In 2-D, SEM meshes are based on quadrangular elements which can easily be generated thanks to standard meshing tools and usually leads to an unstructured mesh. We used the open-source software GMSH (Geuzaine and Remacle, 2009) to generate the mesh and a sample of its geometry is displayed in Fig. 2(c). In each element, we use a degree 6 polynomial approximation per direction. The mesh is generated such that the edge length of each element is not larger than the local minimum wavelength, making sure that the wavefield is well sampled.

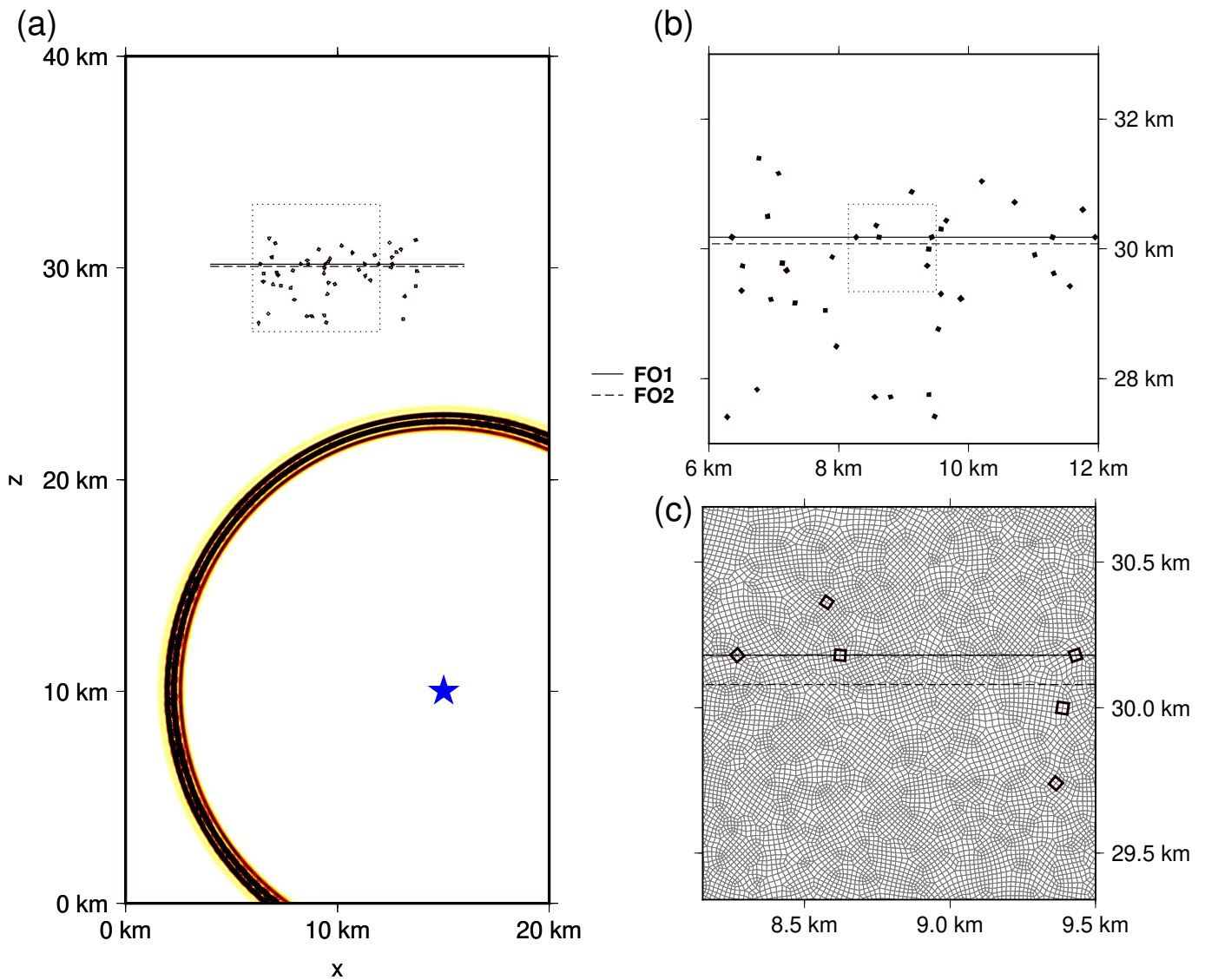


Figure 2 Numerical experiment configuration. (a) global view of the computation domain Ω . The blue star is the source position, the black points are the stone positions and the dotted line square is the zoom area used for the panel (b). The FO cable positions are plotted with the solid (FO1) and the dash (FO2) horizontal lines. A snapshot of the propagating wavefield (its energy density) for $t = 18$ s is also presented. (b) zoom in on the domain around the FOs and stones area. The dotted line square is the zoom area used for panel (c). (c) zoom in on the domain closer to the cables. The black squares are the stones in the area and the grey lines are the SEM element boundaries.

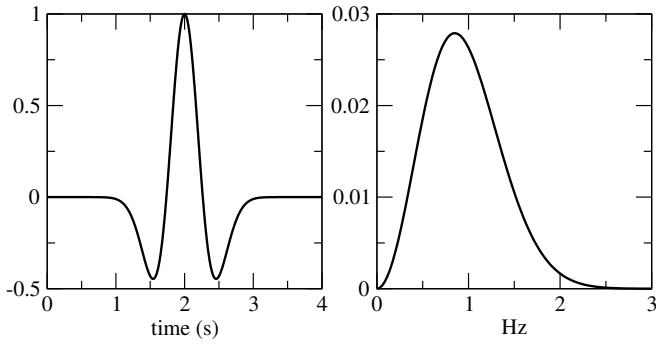


Figure 3 The Ricker source time function $g(t)$ (left panel) and its amplitude spectra (right panel) used for the numerical tests.

In the rest of the paper, we will use the displacement and strain fields instead of the particle velocity and strain rate. This helps to simplify the notations and it is fully equivalent. Indeed, for our modeling, we are using a Ricker source time function g , whereas, for an earthquake-like source time function, we should rather use a Ricker for the source time function rate \dot{g} . Hence, if the source used in our simulation is an earthquake, our results in displacement should be interpreted as velocity and, those in strain as strain rate.

4.1 Numerical experiment observations

In Fig. 4 are shown the displacement u_x and the discrete strain $\Delta_x u_x$ as a function of x and time t along a part of FO1. For both u_x and $\Delta_x u_x$, the first and most energetic arrival is the ballistic P wave followed by the scattered field generated by the stones. On the displacement field, the presence of stones can be seen through the scattered field after the ballistic wave, but the fact that some of them are directly on the cable has no or little impact. On the discrete strain field $\Delta_x u_x$, it is different: seven stones are in contact with the FO cable, and at each contact location, a strong glitch is visible at all times. This observation is similar to what is often seen in real DAS measurements and previously illustrated in section 3.

In Fig. 5, we use a trace collection representation of the same fields, using a normalization trace by trace maximum and zoomed on a smaller portion of the cable. Similarly, the impact of the stones directly in contact with the cable (3 on this cable portion) is barely visible on u_x and obvious on $\Delta_x u_x$. It can be seen that a time arrival series measured from $\Delta_x u_x$ would be strongly perturbed by the presence of the stones, which wouldn't be the case on u_x .

In Fig. 6 is shown u_x and $\Delta_x u_x$ as a function of x for a given time $t = 27.54$ s. The presence of the stones is visible on both fields, but their impact is much larger on $\Delta_x u_x$ than on u_x .

Finally, in Figs. 7 and 8, we display some of the same observations as above but for the FO2. FO2 is parallel to FO1 and offset by -100 m along \hat{z} such that it is not in contact with any stone. It is nevertheless close to the same seven stones lying on the FO1 cable and some others (within a distance lower than $1/10^{\text{th}}$ of λ_{min}). It

can be seen that the effect on the stones on $\Delta_x u_x$ is not as strong as for the FO1, but still noticeable, suggesting that their effect decays quickly with distance but is not purely local.

To conclude this section, we observe two types of spatial variations of the measurements along the FO cables: variations at the scale of the minimum of wavelength λ_{min} and variations at the scale of the size of the stones, or, more precisely, at the scale of the gauge length L_G . In the following, we refer to the first type of variation as “smooth” and to the latter as “rough”. From the point of view of a seismologist, who usually works with displacement fields (or velocities or accelerations), rough variations of the wavefield in the far field are not expected. Indeed, waves are subject to a dispersion relation, typically $\lambda_{\text{min}} = V_{S,\text{min}}/f_{\text{max}}$ in homogeneous media, and we do not expect spatial variations of the wavefield smaller than λ_{min} . This observation, together with the fact that the rough variations are only seen on the strain and not on the displacement, needs to be understood. In the following sections, we rely on the homogenization theory to do so.

5 Theoretical understanding of the small-scales effect on DAS measurements based on the homogenization theory

The objective of this section is to show that

$$\epsilon^{\text{DAS}}(\mathbf{x}, t) = \epsilon_{xx}^*(\mathbf{x}, t) + [\mathbf{J}(\mathbf{x}) : \epsilon^*(\mathbf{x}, t)]_{xx}, \quad (7)$$

where \mathbf{x} is the position along the FO, ϵ^* is the strain tensor computed in the “best possible effective model” and \mathbf{J} is a coupling tensor that is independent of time and type of seismic source. Here, the “best possible effective model” refers to a tomographic model that is good enough to explain the particle displacement or velocity at the DAS measurement positions. In the following, we show that the coupling tensor \mathbf{J} depends only on the fine-scale heterogeneities near the FO. Eq. (7) carries two important information that might not be intuitive for seismologists used to working with local displacement measurements:

1. the DAS measurement is not just the component of the strain tensor along the fiber axis $\epsilon^{\text{DAS}}(\mathbf{x}, t) = \epsilon_{xx}^*(\mathbf{x}, t)$ but involves a term which depends on the other components of the strain tensor,
2. that this contamination by other components of the strain tensor varies at the scale of the heterogeneities and not at the scale of the wavelength.

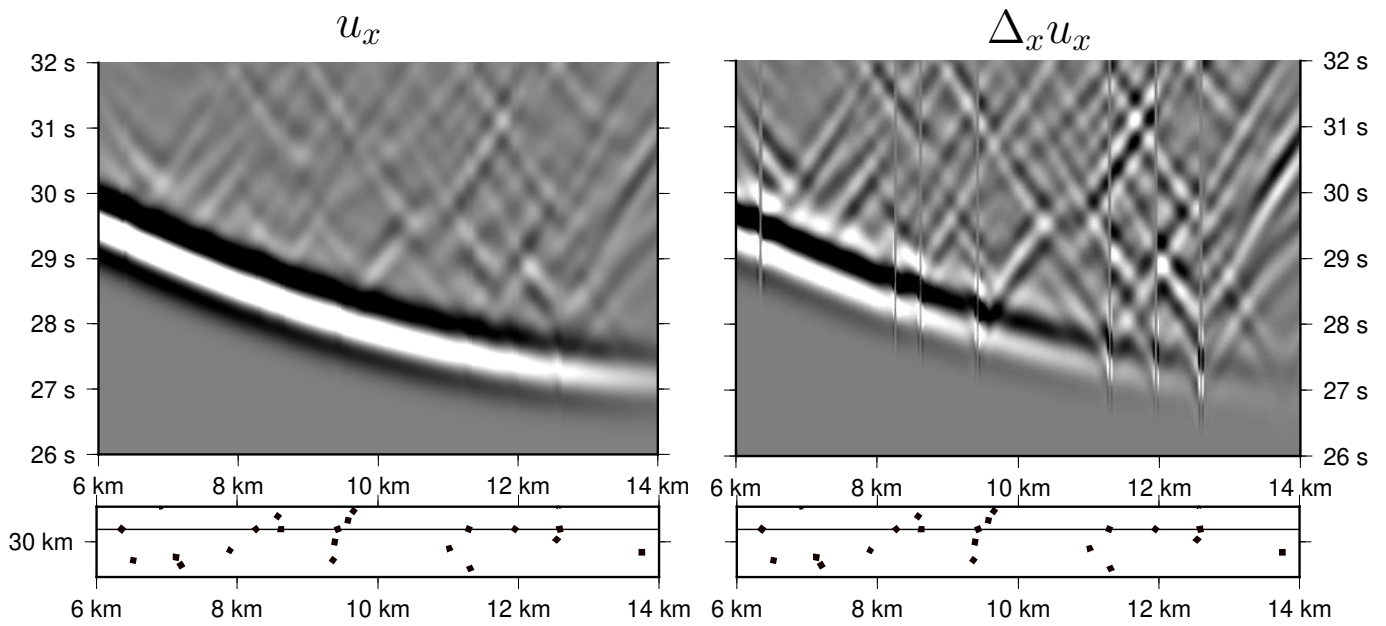


Figure 4 Displacement and strain for FO1. Top left: $u_x(x, z_c, t)$ amplitude. Top right: $\Delta_x u_x(x, z_c, t)$ amplitude. Both maps' amplitude are normalized by their respective maximum. The gray color scale shows negative values in white and positive ones in black. The horizontal axis is the x coordinate and the vertical axis is time. $x = 4$ km is the left origin of the cable. Bottom left and right: (x, z) map of the stone positions (black squares) nearby FO1 (black line).

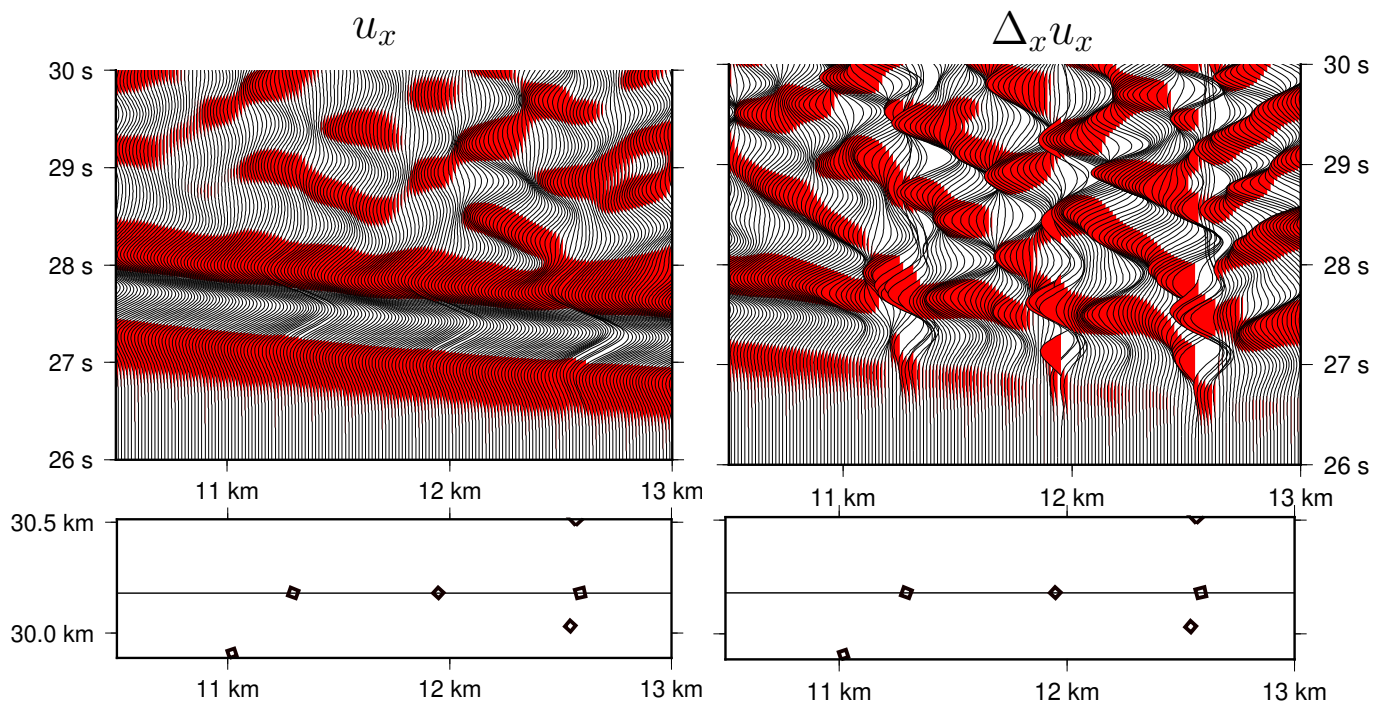


Figure 5 Displacement and strain for FO1 plotted as traces collections. Top left: $u_x(x_i, z_c, t)$ plotted as time traces for the x_i measurement points along the fiber. Top right: $\Delta_x u_x(x_i, z_c, t)$ as time traces. Each trace is normalized by its maximum amplitude. The horizontal axis is the x coordinate and the vertical axis is time. Bottom left and right: (x, z) map of the stone positions (black squares) near FO1 (black line).

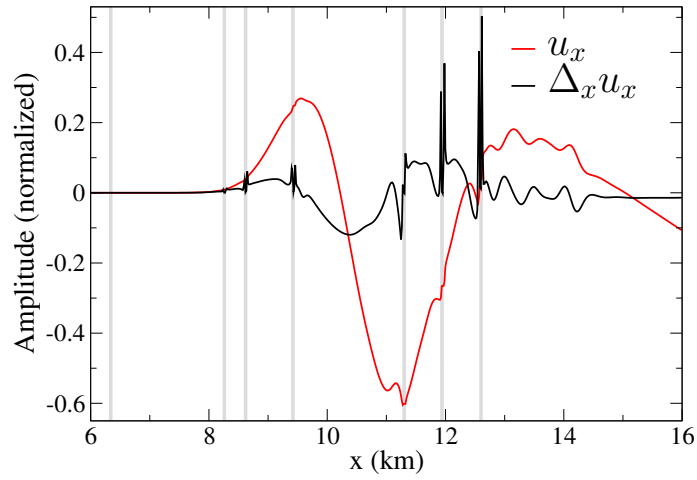


Figure 6 u_x and $\Delta_x u_x$ along a portion of the FO1 line for $t = 27.54$ s. Both field amplitudes are normalized by their respective absolute maximum amplitude. The vertical gray lines show the positions of the stones in contact with FO1.

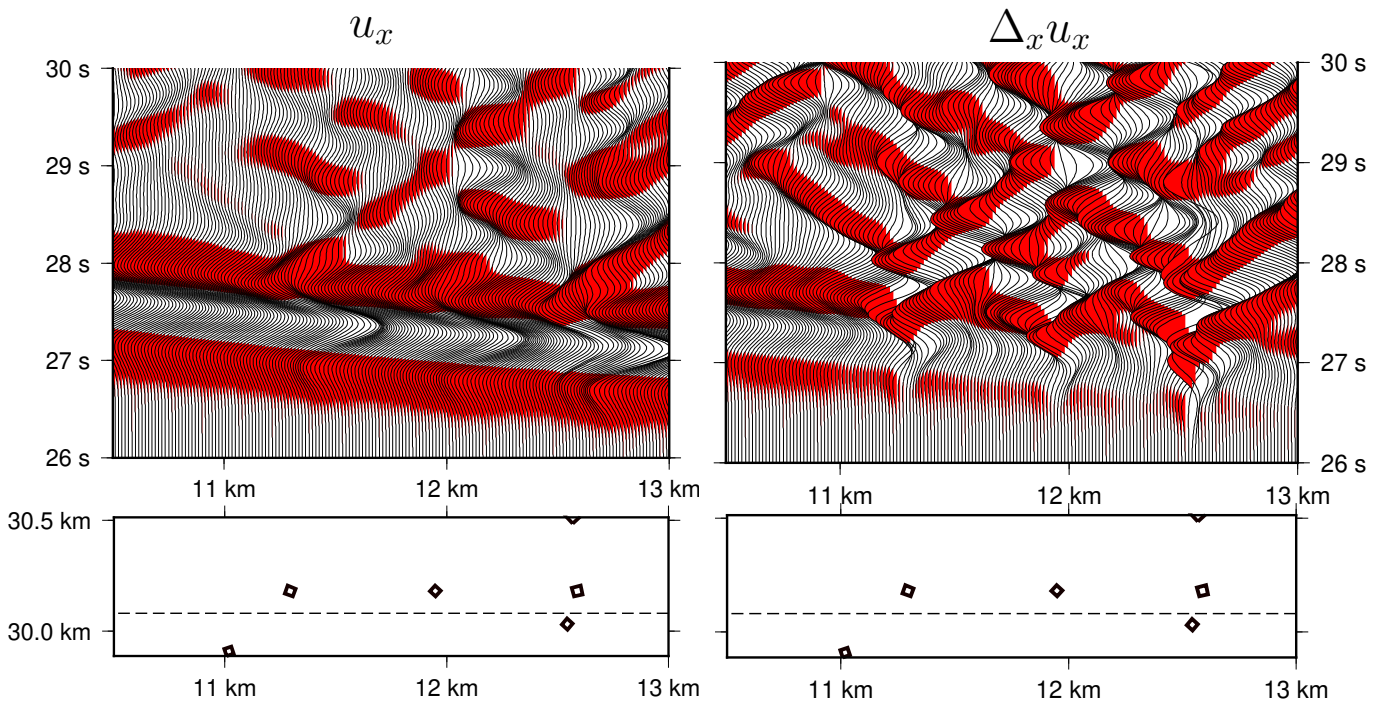


Figure 7 Displacement and strain for a portion of FO2 plotted as traces collections. Top left: $u_x(x_i, z_c, t)$ plotted as time traces for the x_i measurement points along the fiber. Top right: $\Delta_x u_x(x_i, z_c, t)$ as time traces. For both plots, each trace is normalized by its maximum amplitude. The horizontal axis is the x coordinate and the vertical axis is time. Bottom left and right: (x, z) map of the stone positions (black squares) near FO2 (dash line).

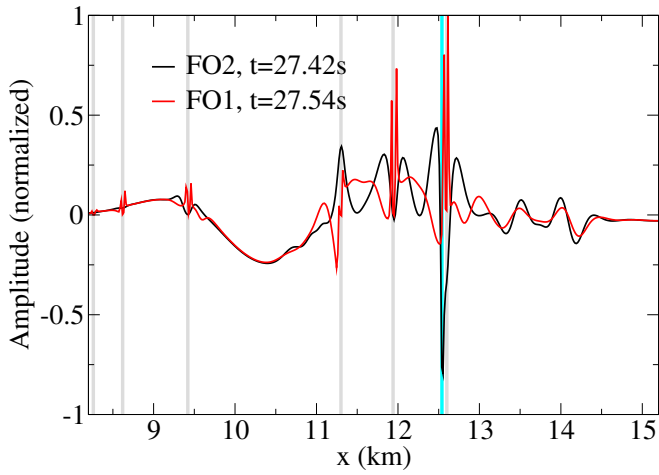


Figure 8 $\Delta_x u_x$ along a portion of FO1 for $t = 27.54$ s and along FO2 for $t = 27.42$ s. The two traces are normalized by the same factor, which is the FO1 maximum amplitude. The vertical gray lines indicate the positions of the stones in contact with FO1. The vertical cyan line indicates the position of the nearest stone to FO2 but not in contact with it. This stone is visible in Fig. 7, lower panels, close to $x = 12.54$ km.

5.1 The homogenization method principle

The two-scale homogenization method deals with obtaining macroscopic (also called homogenized or effective) equations for systems with microscopic structures (Bensoussan et al., 1978; Sanchez-Palencia, 1980). In seismology, a microscopic medium is characterized by spatial variations of its mechanical properties at scales much smaller than the minimum wavelength. By using homogenization, all these microscopic structures are smoothed out, that is the medium with rapidly varying structures can be substituted with another one where the structures are only slowly varying without changing the solution to the wave equation (but with an error that can be controlled). To this end, homogenization has been beneficial in the forward problem to study wave propagation in a fine-layered media (Backus, 1962; Capdeville and Marigo, 2007), to allow sparser meshing to gain computational speed (Capdeville et al., 2010; Cupillard and Capdeville, 2018; Capdeville et al., 2020), as well as in the inverse problem to help interpret the results of full waveform inversion (Capdeville et al., 2013; Capdeville and Métivier, 2018). Due to its ability to explain the interaction between the wavefield and different scales, homogenization is a suitable method to investigate the impact of small-scale structures on DAS measurements, akin to its application in analyzing the interaction of rotational measurements with small-scales (Singh et al., 2020).

Homogenization depends on a small parameter ε defined as

$$\varepsilon = \frac{\lambda}{\lambda_{\min}}, \quad (8)$$

where λ is a wavelength related to the size of the considered heterogeneities (and λ_{\min} the background minimum wavelength as previously defined). Even if it doesn't need to be the case in general, we can assume here that λ is tied to the stone size: the smallest are the

stones the smallest is ε . Please note that no scale separation is required to use the homogenization theory and λ could be a user-defined resolution and is unrelated to the actual media heterogeneity size distribution (see Capdeville et al., 2020).

The homogenization theory also relies on a second space variable, the microscopic scale variable defined as

$$\mathbf{y} = \frac{\mathbf{x}}{\varepsilon}. \quad (9)$$

\mathbf{y} is designed to explicitly manage small-scales while macroscopic scales are handled by the classical space variable \mathbf{x} , also referred to as the macroscopic space variable. \mathbf{y} is a new space variable which, in the two-scale homogenization theory, is treated as independent from \mathbf{x} such that any field depending on both \mathbf{x} and \mathbf{y} depends on 4 space dimensions in 2-D and 6 in 3-D. It shall not be confused with a y -axis, which we don't use in this work.

Homogenization is an asymptotic theory where the displacement depends on both \mathbf{x} and \mathbf{y} and is thought of as a power series in ε :

$$\mathbf{u}^\varepsilon(\mathbf{x}, \mathbf{y}, t) = \mathbf{u}^*(\mathbf{x}, \mathbf{y}, t) + \varepsilon \mathbf{u}^1(\mathbf{x}, \mathbf{y}, t) + \varepsilon^2 \mathbf{u}^2(\mathbf{x}, \mathbf{y}, t) + \dots, \quad (10)$$

where the homogenized coefficients \mathbf{u}^i need to be found. The strain can also be expanded as a power series in ε :

$$\boldsymbol{\epsilon}^\varepsilon(\mathbf{u})(\mathbf{x}, \mathbf{y}, t) = \boldsymbol{\epsilon}^0(\mathbf{x}, \mathbf{y}, t) + \varepsilon \boldsymbol{\epsilon}^1(\mathbf{x}, \mathbf{y}, t) + \varepsilon^2 \boldsymbol{\epsilon}^2(\mathbf{x}, \mathbf{y}, t) + \dots, \quad (11)$$

where the $\boldsymbol{\epsilon}^i$ are the strain homogenized expansion coefficients. Please note that, in the last two equations, the exponent i is a power for ε and an index for \mathbf{u}^i and $\boldsymbol{\epsilon}^i$.

The main results of the homogenization development are the following:

1. to the leading order (in ε), the displacement is independent of the small-scale variable \mathbf{y} :

$$\mathbf{u}^*(\mathbf{x}, \mathbf{y}, t) = \mathbf{u}^*(\mathbf{x}, t). \quad (12)$$

2. the order 1 homogenized coefficient can be written as

$$\mathbf{u}^1(\mathbf{x}, \mathbf{y}, t) = \boldsymbol{\chi}(\mathbf{x}, \mathbf{y}) : \boldsymbol{\epsilon}^*(\mathbf{x}, t) + \langle \mathbf{u}^1 \rangle(\mathbf{x}, t), \quad (13)$$

where $\boldsymbol{\epsilon}^* = \boldsymbol{\epsilon}(\mathbf{u}^*)$, $\boldsymbol{\chi}$ is the first order corrector (a third order tensor) and where $\langle \mathbf{u}^1 \rangle$ can be, in general, neglected. $\boldsymbol{\chi}$ is the solution of a set of equations known as the ‘‘cell problem’’. It is a static elasticity-style of equations with a set of source terms (Capdeville et al., 2010, 2015). It depends only on the elastic model and neither on time nor on the seismic source.

3. to the leading order, the strain depends on the small-scale variable \mathbf{y} :

$$\boldsymbol{\epsilon}^0(\mathbf{x}, \mathbf{y}, t) = (\mathbf{I} + \boldsymbol{\epsilon}_y(\boldsymbol{\chi})(\mathbf{x}, \mathbf{y})) : \boldsymbol{\epsilon}^*(\mathbf{x}, t), \quad (14)$$

where \mathbf{I} is the fourth order identity tensor and, for any \mathbf{v} , $[\boldsymbol{\epsilon}_y]_{ij}(\mathbf{v}) = \frac{1}{2}(\partial_{y_i} v_j + \partial_{y_j} v_i)$.

4. It can be shown that the equation driving \mathbf{u}^* is also a wave equation but based on the effective elastic tensor \mathbf{c}^* and density ρ^* and not on the true (fine-scale) mechanical properties (ρ, \mathbf{c}) . Moreover, \mathbf{c}^* can be obtained from χ . The relation of the solution χ to the elastic properties is non-linear making the homogenization results often non-intuitive. For example, the effective properties are almost always anisotropic even if the true model is isotropic. Solving the cell problem and then finding the effective mechanical properties, in general, involves a numerical solver. Only the layered medium case leads to an analytical solution. In the latter case, the homogenization theory falls back to the results of [Backus \(1962\)](#). We do not expand more on this aspect as it is not required for our discussion and refer to [Capdeville et al. \(2020\)](#) for complete development.

The order 1 effective homogenized displacement is

$$\mathbf{u}^\varepsilon(\mathbf{x}, \mathbf{y}, t) = \mathbf{u}^*(\mathbf{x}, t) + \varepsilon \chi(\mathbf{x}, \mathbf{y}) : \boldsymbol{\epsilon}^*(\mathbf{x}, t), \quad (15)$$

and the order 0 effective strain tensor is

$$\boldsymbol{\epsilon}^\varepsilon(\mathbf{x}, \mathbf{y}, t) = (\mathbf{I} + \boldsymbol{\epsilon}_y(\chi)(\mathbf{x}, \mathbf{y})) : \boldsymbol{\epsilon}^*(\mathbf{x}, t). \quad (16)$$

The relation between the true fields and the effective fields as defined above are

$$\mathbf{u}(\mathbf{x}, t) = \mathbf{u}^\varepsilon(\mathbf{x}, \mathbf{y} = \frac{\mathbf{x}}{\varepsilon}, t) + O(\varepsilon^2), \quad (17)$$

$$\boldsymbol{\epsilon}(\mathbf{x}, t) = \boldsymbol{\epsilon}^\varepsilon(\mathbf{x}, \mathbf{y} = \frac{\mathbf{x}}{\varepsilon}, t) + O(\varepsilon). \quad (18)$$

Please note that it is possible to also define the strain at the order 1, but it is not necessary for the present study.

5.2 Homogenization applied to DAS cable measurement

In this section, we assume the DAS interrogator is measuring the strain in the cable direction, that is $\Delta_x u_x = \partial_x u_x = \epsilon_{xx}$ which is true for $L_G \rightarrow 0$. This is in general not true as the DAS gauge length L_G is typically of several meters. Nevertheless, we show in appendix A that the fact that the gauge length is finite doesn't affect our conclusions.

Based on the previous section, to the order 1 in displacement and to the leading order in strain, we have

$$u_x(\mathbf{x}, t) = u_x^*(\mathbf{x}, t) + \varepsilon \chi_{xij}(\mathbf{x}, \mathbf{y}) \epsilon_{ij}^*(\mathbf{x}, t) + O(\varepsilon^2), \quad (19)$$

$$\epsilon_{xx}(\mathbf{x}, t) = \epsilon_{xx}^*(\mathbf{x}, t) + \Xi_{xxij}(\mathbf{x}, \mathbf{y}) \epsilon_{ij}^*(\mathbf{x}, t) + O(\varepsilon), \quad (20)$$

where, in the two last equations, $\mathbf{y} = \mathbf{x}/\varepsilon$ and $\Xi = \boldsymbol{\epsilon}_y(\chi)$. Please note that $\boldsymbol{\epsilon}^*$ is different from $\boldsymbol{\epsilon}^0$ as defined in eq. (11) and solved in eq. (14): $\boldsymbol{\epsilon}^*$ is the strain associated to the order 0 effective displacement \mathbf{u}^* which means it is a smooth quantity, and only depends on \mathbf{x} . On the contrary, $\boldsymbol{\epsilon}^0$, the order 0 effective strain, is a rough quantity and depends on both \mathbf{x} and \mathbf{y} .

Eq. (20) demonstrates eq. (7) with $J_{ij}(\mathbf{x}) = \Xi_{xxij}(\mathbf{x}, \mathbf{x}/\varepsilon)$. Moreover, eqs. (19) and (20) are sufficient to interpret the numerical observations made in Sec. 4.1. On the one hand, u_x^* and $\boldsymbol{\epsilon}^*$ only depend

spatially on the macroscopic variable \mathbf{x} . Within the homogenization theory, this fact implies that those quantities are spatially smooth: their spatial variations are tied to λ_{\min} and cannot be smaller than λ_{\min} . This means that, if we lower the signal maximum frequency f_{\max} , because it implies a larger λ_{\min} , then u_x^* and $\boldsymbol{\epsilon}^*$ will show spatially smoother variations. On the other hand, the corrector χ and its gradient Ξ also depend on the microscopic variable \mathbf{y} . Within the homogenization theory, this fact implies that those quantities are spatially rough: their spatial variations are mainly tied to the geometry of the heterogeneities and, remarkably, changing f_{\max} does not affect those rough spatial variations.

We can now look at the interaction between the small-scale heterogeneities with the displacement and strain measurements along a FO. Knowing that the correction terms (the product of the corrector with the strain $\chi : \boldsymbol{\epsilon}^*$ for the displacement field and the product of the corrector gradient with the strain $\Xi : \boldsymbol{\epsilon}^*$ for the strain field) are rough quantities, we have:

- On the displacement field, the correction is of order 1, that is with a leading ε (the small parameter defined in eq. (9)). This implies that this correction is small in amplitude, and even more so that the heterogeneity is small with respect to λ_{\min} . This result is compatible with the observations made in the left panels of Fig. 4-5, and in Fig. 6: the u_x displacement display spatial variations at the scale of λ_{\min} and only a small impact of the stones can be noticed,
- On the strain field, the correction is of leading order: it has no leading ε . In contrast to the displacement, this implies that the correction is of large amplitude and is not related to the size of heterogeneities: for a given mechanical property contrast, a spatially small or large heterogeneity has a similar amplitude effect on the strain. A numerical illustration of this non-intuitive effect is given in [Capdeville et al. \(2020\)](#), Figs. 6 and 9. This is compatible with the observation made in the right panels of Fig. 4-Fig. 5, and in Fig. 6: the strain ϵ_{xx} displays large amplitude spatial variations at the scale of stone size (much smaller than λ_{\min}) on top of smooth variations.

5.3 A numerical application of the homogenization theory applied to DAS

In this section, we apply the homogenization theory developed in the two previous sections to the results of the numerical experiment presented in Sec. 4.1.

Knowing the true media mechanical properties (ρ, \mathbf{c}) and assuming $\lambda_{\min} = 200$ m, we compute the effective mechanical properties (ρ^*, \mathbf{c}^*) following the homogenization procedure described in [Capdeville et al. \(2010\)](#) and using $\varepsilon = 1$. In practice, ε is a user-defined value and $\varepsilon = 1$ implies that the heterogeneity scales of size smaller than λ_{\min} are removed. To obtain a good match between the order 0 effective displacement \mathbf{u}^* , obtained by solving the wave equation using (ρ^*, \mathbf{c}^*) , and the true

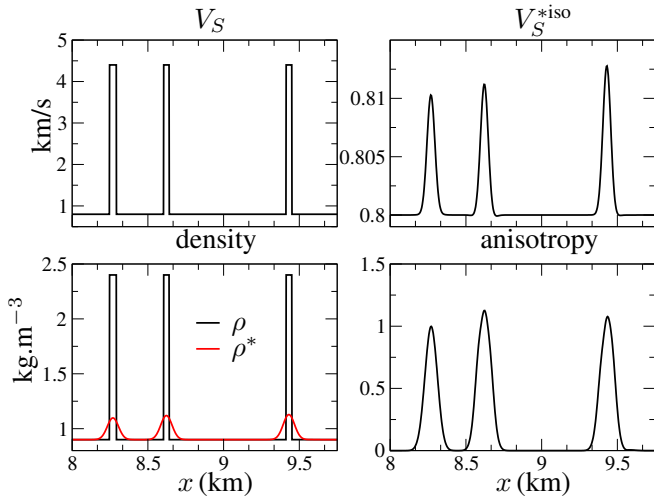


Figure 9 Sample of a cross-section in the 2-D of the effective media used in Sec. 5.3, along the FO1 in the [8, 9.7] km range. Upper left panel: V_S in the original media. Upper right panel: isotropic S-velocity projection from the effective media V_S^{*iso} . Lower left panel: original density (ρ) and effective density (ρ^*). Lower right panel: total anisotropy (in %) in the effective media

displacement \mathbf{u} , it has been shown that $\varepsilon = 0.5$ is good enough for most media (Capdeville et al., 2010). Nevertheless, a smaller value for ε (from 0.25 to 0.1) may be necessary for strongly scattering media or long signals (Mizuno et al., 2020). Therefore, using $\varepsilon = 1$ in our example, we know that the effective media is not detailed enough to accurately model the coda wave, but it is sufficient for the ballistic P-wave. Moreover, using an $\varepsilon > 0.5$ corresponds to the most realistic situation where the background velocity model is, at best, known with a poor resolution. For more discussions about the relationship between effective media and tomographic media, one can refer to Capdeville and Métivier (2018). We illustrate some components of the effective properties, and how they relate to those of the original medium, in Fig. 9.

As aforementioned, the effective media turns out to be almost always fully anisotropic, even if the true medium is isotropic. To represent this anisotropy of the medium, we first compute the isotropic projection elastic tensor \mathbf{c}^{*iso} of the effective elastic tensor \mathbf{c}^* following Browaeys and Chevrot (2004). Then, we plot in Fig. 9, the effective isotropic S-velocity V_S^{*iso} computed from \mathbf{c}^{*iso} , the total anisotropy (the matrix distance between \mathbf{c} and \mathbf{c}^{*iso} relative to the norm of \mathbf{c}^{*iso}), ρ and ρ^* . We can now visualize that the maximum amplitude of V_S^{*iso} is much smaller than the one of V_S , implying that some induced anisotropy has been created. This is one of the non-linear and non-intuitive effects of the homogenization process.

An example comparing horizontal displacement traces for a receiver located near the middle of FO1, obtained in the true medium and in the effective media is given in Fig. 10. As expected, the ballistic P-wave arrival is well modeled by the effective media whereas the coda wave is poorly modeled. An accurate modeling could be reached by lowering ε as it is done in Capdeville et al.

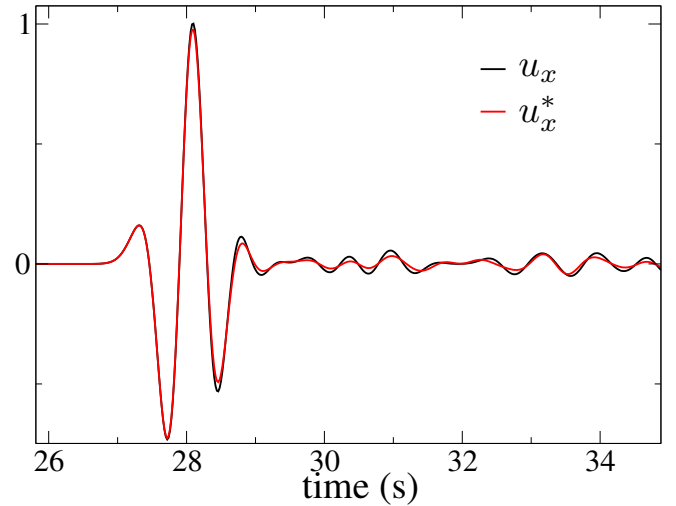


Figure 10 Displacement traces for a receiver located in (10 km, 30.18 km) (on the FO1) computed in the true media (u_x) and in the $\varepsilon = 1$ effective medium (u_x^*). The trace amplitudes have been normalized by the u_x maximum amplitude. The first arrival is the ballistic P-wave followed by the scattered waves from the stones.

(2010) or Mizuno et al. (2020) for examples. Nevertheless, as explained earlier, this is not the point here.

In Figs. 11b and 11d, we compare the true horizontal displacement u_x recorded along FO1, to the order 0 effective displacement u_x^* and the order 1 effective displacement $u_x^* + \varepsilon \chi_{xij} \epsilon_{ij}^*$, respectively. It shows an overall good match between the true solution and the effective ones. Moreover, the order 1 correction to the order 0 effective displacement makes little difference. This is coherent with the fact that the correction is of order 1, which is small if the heterogeneity structures are small compared to the minimum wavelength. In other words, the recorded displacement is dominated by propagating waves and not some local effect near the sensor. Figs. 11a and 11c show a similar comparison but for $\Delta_x u_x$. Before going further, we need to account for the fact that L_G is finite, which was not done in Sec. 5.2. To the order 1 in L_G , if $L_G \ll \lambda_{min}$, $\partial_x = \Delta_x$ only for smooth quantities. For example, this is true for u_x^* but not for u_x . To the order 1 in L_G , we therefore have $\epsilon_{xx}^* = \partial_x u_x^* = \Delta_x u_x^*$ but $\Delta_x u_x \neq \partial_x u_x$. In the end, as shown in Appendix A, we obtain for $\Delta_x u_x$ a solution very similar to eq. (20) but replacing Ξ by its finite difference formula $\tilde{\Xi}$ given in eq. (28) to obtain

$$\Delta_x u_x(x, t) = \epsilon_{xx}^*(\mathbf{x}, t) + \tilde{\Xi}_{xxij} \epsilon_{ij}^*(\mathbf{x}, t) + O(\varepsilon, L_G). \quad (21)$$

Please note that, in the general case where the medium is not smooth at the L_G scale, $\tilde{\Xi}$ and Ξ are different. Nevertheless, they both only depend on the geometry and mechanical properties of the true fine-scale medium. In Fig. 11a, we see that ϵ_{xx}^* is indeed smooth at the minimum wavelength scale. It matches the DAS measurement $\Delta_x u_x$ away from the stones and they strongly differ near them. In Fig. 11c, we see that, when the corrector $\tilde{\Xi} : \epsilon^*$ is added, the effective solution matches the DAS measurement including nearby the stones. Let's finally mention that, in Figs. 11c and 11d, a better agreement between the effective solution

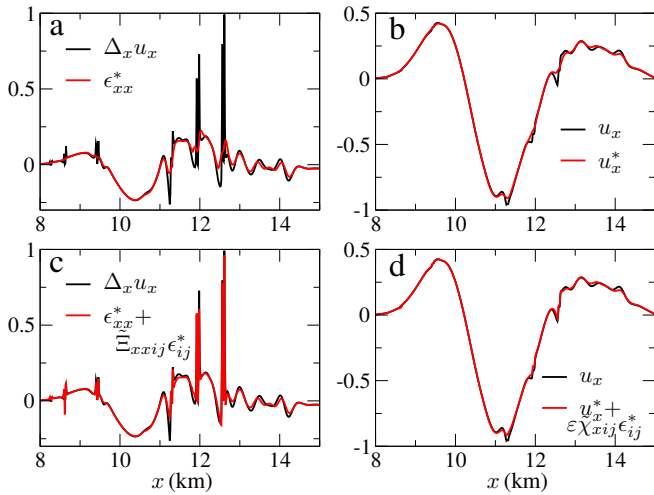


Figure 11 True and effective measurements comparison for FO1. Panel a: reference cable measurement ($\Delta_x u_x$) and strain of the order 0 finite difference effective displacement (ϵ_{xx}^*). Panel b: displacement (u_x) and order 0 effective displacement (u_x^*). Panel c: reference cable measurement ($\Delta_x u_x$) and the order 0 effective strain ($\epsilon_{xx}^* + \Xi_{xxij} \epsilon_{ij}^*$). Panel d: displacement (u_x) and order 1 effective displacement ($u_x^* + \epsilon_{\chi_{xij}} \epsilon_{ij}^*$). For each panel, the amplitudes have been normalized by the absolute maximum amplitude of the signal.

and the true solutions could be obtained by simply using a smaller ϵ .

6 Discussion

In section 3, after some simple filtering and technical considerations, we have shown that field DAS measurements can display anomalies: short distance spatial changes in the recorded wavefield that are not compatible with wave propagation and its dispersion relation. Such anomalies can be attributed to abrupt changes in the soil-cable coupling conditions or changes in the cable direction. In this work, we have shown that small-scale heterogeneities near the fiber optics can have a strong effect and are another possibility also able to explain such anomalies. Whenever possible, trenching of cables onland and offshore is done in homogeneous soft soils to simplify the operations and optimize coupling. Under these conditions, the impact of small-scale anomalies can be limited. However, cables installed for telecom, whether it is on land or offshore, are likely encountering numerous small-scale heterogeneities and abrupt changes in the coupling conditions (cable passing a bridge, an underwater canyon, migration of seafloor sediments covering or uncovering cable sections...).

We have numerically tested the effects of these small-scale heterogeneities on DAS measurements. In those tests, we have used only simple square shape stiff heterogeneities in a simple 2-D setting, but were able to reproduce key characteristics of the DAS measurements (e.g. high wavenumber signatures mostly insensitive to temporal filtering). We expect other shapes, other velocity contrasts (e.g. soft heterogeneities), and other lo-

cations (e.g. near the free surface), 3-D and free surface effects to produce a wide range of different effects on DAS measurements. Nevertheless, thanks to the homogenization arguments employed here, we know that what matters is the fact that a DAS is measuring a component of the spatial gradient of the wavefield. Hence, we anticipate a significant impact from the various types of heterogeneities, including free surface fine-scale topography (Capdeville and Marigo, 2013), surpassing that on the displacement field. However, a comprehensive investigation is still needed to precisely determine the extent to which small-scales affect DAS measurements.

Some practical aspects of the DAS measurements about the laser pulse width and the fact that measurements are often overlapping (the number of measurements is larger than the FO length divided by the gauge length) have not been accounted for. Nevertheless, if these details have an impact on the exact shape of Ξ and its formula, it doesn't change the overall conclusion of this work. Taking into account these different details of the DAS measurements would not change the overall strain components coupling.

If our study has been carried out in 2-D, a very similar result would be found in 3-D. Indeed, similar correctors and coupling effects are obtained in 3-D (Cupillard and Capdeville, 2018). Small-scale topography also leads to similar effects (Capdeville and Marigo, 2013). Therefore, we expect that going to 3-D or including topography would not change the overall message of this work.

The overall message of the present work is that DAS measurements sensitivity to nearby heterogeneities of scale much smaller than the minimum wavelength is much higher than for displacement, velocity, or acceleration measurements. Our numerical experiments as well as our theoretical development based on homogenization show that this sensitivity is characterized by a coupling of the different components of the strain (rate) localized in the vicinity of each heterogeneity. This result is compatible with the correlation of DAS and array strain measurement differences with surface geology observed in data (Muir and Zhan, 2022). This is also compatible with the observed rotational-strain coupling due to small-scale topography and heterogeneity (van Driel et al., 2012; Singh et al., 2020).

When using DAS data, these small-scale interactions can be both bad or good news depending on the objective. On the bad side, the fact that DAS measurements are very sensitive to small local heterogeneities is a problem for most seismic wave applications based on wave propagation such as tomographic methods of any kind. Indeed, imaging the earth's interior at all scales is out of reach and every tomographic method needs a non-zero minimum resolution to make the inverse problem tractable. In the case of displacement measurements, it is possible to find this minimum resolution because displacement is a smooth quantity which, in the homogenization framework, means that only depends on x (at least at the leading order) and on the effective mechanical properties. Therefore, if we have no hope of finding the true mechanical properties at

all scales, we can find the effective mechanical properties. Indeed, we know by construction that the effective mechanical properties have a non-zero minimum resolution, and we can show that a tomographic method can find, at best, the effective properties of the earth (Capdeville and Métivier, 2018). In other words, a tomographic method needs the effective displacement \mathbf{u}^* as data because it only depends on (ρ^*, \mathbf{c}^*) , which is tractable for an inverse problem. In practice, we can still use the true displacement \mathbf{u} as data because it happens that it is a good approximation of \mathbf{u}^* ($\mathbf{u} = \mathbf{u}^*$ to the leading order in ε). Unfortunately, we cannot say the same thing about $\Delta_x u_x$, as measured by DAS interrogators, which is a bad approximation of ϵ_{xx}^* . This implies that, to explain $\Delta_x u_x$ data, we should invert for (ρ, \mathbf{c}) at all scales, which is impossible. Moreover, in practical terms, it implies that the summation of x neighboring DAS channels may not be equivalent to data acquired with a gauge length x times larger. Nevertheless, as we have seen it here, the sensitivity to the small-scale y is only for the small heterogeneities near the sensor. In the case of rotational sensors, it has been suggested to invert for the corrector $\bar{\Xi}$ at the sensor location together with the tomographic image (Singh et al., 2020). It is probably possible to do the same for DAS campaigns, but it will be more difficult as a single DAS campaign implies inverting for many coupling correctors (one for every L_G), compared to one per sensor in the case of a rotational instrument. Therefore, the path to use DAS in tomography with the same level of accuracy as for displacement sensors remains to be shown. Another type of method for which the DAS sensitivity to small local heterogeneities is a problem is source localization. Indeed, ignoring these effects might lead to biased estimates.

On the good side, the fact that DAS is a very sensitive instrument to small-scales makes it a great tool to detect heterogeneities near the cable at the L_G scale and not at the λ_{\min} scale. Many applications can be imagined based on this sensitivity such as fault detection with DAS in boreholes to localization of seafloor lost electric or Internet cables. Moreover, it is possible to determine some of the small-scale mechanical properties at the L_G scale from the determined corrector $\bar{\Xi}$ components which would be of great interest. In both cases, how to mitigate these effects or how to use them in practice remains to be studied in future works.

7 Conclusion

We have shown that heterogeneities of scales much smaller than the minimum wavelength can have a strong effect on DAS measurements leading to a coupling of the different strain components. In the data, these small-scale heterogeneities should appear as relatively independent of the type of temporal filtering applied and not follow the classical dispersion relationship. We explain this effect by the fact that DAS is measuring a quantity that is close to a component of the strain and that it can be shown that, using the homogenization theory, small heterogeneity scales have a much stronger effect on the wavefield gradients than on the

wavefield itself. This effect can be perceived as both advantageous (e.g. for detecting small structures) and disadvantageous (e.g. for conducting tomography inversion or locating seismic sources) depending on the type of application.

Acknowledgements

We thank the two anonymous reviewers and the associate editor, Stephen Hicks, for their constructive comments that helped us to improve the manuscript. We thank Sneha Singh, Olivier Sebe and Amaury Vallage for valuable discussions about this coupling effect and DAS data. We thank Heiner Igel, for organizing his amazing winter school “skience” during which the two authors had their first discussion about this topic. Numerical modeling computations were performed thanks to the GLiCID computing center resources. The DAS measurements were acquired thanks to the help of the people in charge of the Ardèche Drôme Numérique telecom network, and of the ADTIM company managing the network. We are grateful to the FEBUS Optics team for providing a DAS interrogator unit promptly after the 2019 Mw4.3 Le Teil earthquake. A.S. was partly supported by the SEAFOOD project, funded in part by the grant ANR-17-CE04-0007 of the French Agence Nationale de la Recherche. This work was also partly funded by the ASIRIplus_SD ANR-19-CE22-0015 project and has benefited from discussions within SPIN ITN (from the European Commission under the Horizon 2020 Marie Skłodowska-Curie Action (MSCA)) project.

Data and code availability

The data used in this work can be found here: <https://doi.org/10.5281/zenodo.7875052>. SPEC2DY, the 2-D spectral element codes used in the present work can be found here: <https://gitlab.univ-nantes.fr/capdeville-y/spec2dya>.

Competing interests

The authors have no competing interests.

References

- Backus, G. Long-Wave Elastic Anisotropy Produced by Horizontal Layering. *J. Geophys. Res.*, 67(11):4427–4440, 1962. doi: 10.1029/JZ067i011p04427.
- Baker, M. G. and Abbott, R. E. Rapid Refreezing of a Marginal Ice Zone Across a Seafloor Distributed Acoustic Sensor. *Geophysical Research Letters*, 49(24):e2022GL099880, 2022. doi: 10.1029/2022GL099880.
- Bakku, S. K. *Fracture Characterization from Seismic Measurements in a Borehole*. Thesis, Massachusetts Institute of Technology, 2015.
- Bensoussan, A., Lions, J.-L., and Papanicolaou, G. *Asymptotic Analysis of Periodic Structures*. North Holland, 1978.
- Berger, J. and Beaumont, C. An Analysis of Tidal Strain Observations from the United States of America II. The Inhomogeneous Tide. *Bulletin of the Seismological Society of America*, 66(6): 1821–1846, Dec. 1976. doi: 10.1785/BSSA0660061821.

- Bouffaut, L., Taweessintanon, K., Kriesell, H. J., Rørstadbotnen, R. A., Potter, J. R., Landrø, M., Johansen, S. E., Brenne, J. K., Haukanes, A., Schjelderup, O., and Storvik, F. Eavesdropping at the Speed of Light: Distributed Acoustic Sensing of Baleen Whales in the Arctic. *Frontiers in Marine Science*, 9, 2022. doi: 10.3389/fmars.2022.901348.
- Browaays, J. T. and Chevrot, S. Decomposition of the elastic tensor and geophysical applications. *Geophys. J. Int.*, 159:667–678, 2004. doi: 10.1111/j.1365-246X.2004.02415.x.
- Capdeville, Y. and Marigo, J. J. Second order homogenization of the elastic wave equation for non-periodic layered media. *Geophys. J. Int.*, 170:823–838, 2007. doi: 10.1111/j.1365-246X.2007.03462.x.
- Capdeville, Y. and Marigo, J.-J. A non-periodic two scale asymptotic method to take account of rough topographies for 2-D elastic wave propagation. *Geophys. J. Int.*, 192(1):163–189, 2013. doi: 10.1093/gji/ggs001.
- Capdeville, Y. and Métivier, L. Elastic full waveform inversion based on the homogenization method: theoretical framework and 2-D numerical illustrations. *Geophysical Journal International*, 213(2):1093–1112, 2018. doi: 10.1093/gji/ggy039.
- Capdeville, Y., Guillot, L., and Marigo, J. J. 2D nonperiodic homogenization to upscale elastic media for P-SV waves. *Geophys. J. Int.*, 182:903–922, 2010.
- Capdeville, Y., Stutzmann, E., Wang, N., and Montagner, J.-P. Residual homogenization for seismic forward and inverse problems in layered media. *Geophys. J. Int.*, 194(1):470–487, 2013.
- Capdeville, Y., Zhao, M., and Cupillard, P. Fast Fourier homogenization for elastic wave propagation in complex media. *Wave Motion*, 54:170–186, 2015.
- Capdeville, Y., Cupillard, P., and Singh, S. Chapter Six - An introduction to the two-scale homogenization method for seismology. In Moseley, B. and Krischer, L., editors, *Machine Learning in Geosciences*, volume 61 of *Advances in Geophysics*, pages 217 – 306. Elsevier, 2020. doi: <https://doi.org/10.1016/bs.agph.2020.07.001>.
- Chaljub, E., Komatitsch, D., Capdeville, Y., Vilotte, J.-P., Valette, B., and Festa, G. Spectral Element Analysis in Seismology. In Wu, R.-S. and Maupin, V., editors, *Advances in Wave Propagation in Heterogeneous Media*, volume 48 of *Advances in Geophysics Series*, pages 365–419. Elsevier, 2007. doi: 10.1016/S0065-2687(06)48007-9.
- Cheng, F., Chi, B., Lindsey, N. J., Dawe, T. C., and Ajo-Franklin, J. B. Utilizing Distributed Acoustic Sensing and Ocean Bottom Fiber Optic Cables for Submarine Structural Characterization. *Scientific Reports*, 11(1):5613, Mar. 2021. doi: 10.1038/s41598-021-84845-y.
- Cornou, C., Ampuero, J.-P., Aubert, C., Audin, L., Baize, S., Billant, J., Brenguier, F., Causse, M., Chlieh, M., and Combey, A. Rapid Response to the M 4.9 Earthquake of November 11, 2019 in Le Teil, Lower Rhône Valley, France. *Comptes Rendus. Géoscience*, 353(S1):1–23, 2021. doi: 10.5802/crgeos.30.
- Cupillard, P. and Capdeville, Y. Non-periodic homogenization of 3-D elastic media for the seismic wave equation. *Geophysical Journal International*, 213(2):983–1001, 2018.
- Daley, T. M., Freifeld, B. M., Ajo-Franklin, J., Dou, S., Pevzner, R., Shulakova, V., Kashikar, S., Miller, D. E., Goetz, J., Henningses, J., et al. Field Testing of Fiber-Optic Distributed Acoustic Sensing (DAS) for Subsurface Seismic Monitoring. *The Leading Edge*, 32(6):699–706, 2013. doi: 10.1190/le32060699.1.
- Dean, T., Hartog, A., Cuny, T., and Englich, F. The Effects of Pulse Width on Fibre-Optic Distributed Vibration Sensing Data. In *78th EAGE Conference and Exhibition 2016*, volume 2016, pages 1–5. EAGE Publications BV, 2016. doi: 10.3997/2214-4609.201600684.
- Dean, T., Cuny, T., and Hartog, A. H. The Effect of Gauge Length on Axially Incident P-waves Measured Using Fibre Optic Distributed Vibration Sensing. *Geophysical Prospecting*, 65(1):184–193, 2017. doi: 10.1111/1365-2478.12419.
- Festa, G. and Vilotte, J.-P. The Newmark scheme as velocity-stress time-staggering: an efficient implementation for spectral element simulations of elastodynamics. *Geophys. J. Int.*, 161:789–812, 2005. doi: 10.1111/j.1365-246X.2005.02601.x.
- Geuzaine, C. and Remacle, J.-F. Gmsh: a three-dimensional finite element mesh generator with built-in pre- and post-processing facilities. *Int. J. Num. Methods in Engrg.*, 79:1309–1331, 2009. doi: 10.1002/nme.2579.
- Gomberg, J. and Agnew, D. The Accuracy of Seismic Estimates of Dynamic Strains: An Evaluation Using Strainmeter and Seismometer Data from Piñon Flat Observatory, California. *Bulletin of the Seismological Society of America*, 86(1A):212–220, 1996. doi: 10.1785/BSSA08601A0212.
- Harrison, J. C. Cavity and Topographic Effects in Tilt and Strain Measurement. *Journal of Geophysical Research*, 81(2):319–328, Jan. 1976. doi: 10.1029/JB081i002p00319.
- Hartog, A. H. *An Introduction to Distributed Optical Fibre Sensors*. CRC press, 2017. doi: 10.1201/9781315119014.
- Hubbard, P. G., Vantassel, J. P., Cox, B. R., Rector, J. W., Yust, M. B. S., and Soga, K. Quantifying the Surface Strain Field Induced by Active Sources with Distributed Acoustic Sensing: Theory and Practice. *Sensors*, 22(12):4589, Jan. 2022. doi: 10.3390/s22124589.
- Komatitsch, D. and Vilotte, J. P. The spectral element method: an effective tool to simulate the seismic response of 2D and 3D geological structures. *Bull. Seism. Soc. Am.*, 88:368–392, 1998. doi: 10.1785/BSSA0880020368.
- Kuvshinov, B. Interaction of Helically Wound Fibre-Optic Cables with Plane Seismic Waves: Interaction of Fibre-Optic Cables. *Geophysical Prospecting*, 64(3):671–688, May 2016. doi: 10.1111/1365-2478.12303.
- Lindsey, N. J., Martin, E. R., Dreger, D. S., Freifeld, B., Cole, S., James, S. R., Biondi, B. L., and Ajo-Franklin, J. B. Fiber-Optic Network Observations of Earthquake Wavefields. *Geophysical Research Letters*, 44(23):11,792–11,799, Dec. 2017. doi: 10.1002/2017GL075722.
- Lindsey, N. J., Dawe, T. C., and Ajo-Franklin, J. B. Illuminating Seafloor Faults and Ocean Dynamics with Dark Fiber Distributed Acoustic Sensing. *Science*, 366(6469):1103–1107, Nov. 2019. doi: 10.1126/science.aay5881.
- Lior, I., Mercerat, E. D., Rivet, D., Sladen, A., and Ampuero, J.-P. Imaging an Underwater Basin and Its Resonance Modes Using Optical Fiber Distributed Acoustic Sensing. *Seismological Society of America*, 93(3):1573–1584, 2022. doi: 10.1785/0220210349.
- Lomnitz, C. Frequency Response of a Strainmeter. *Bulletin of the Seismological Society of America*, 87(4):1078–1080, Aug. 1997. doi: 10.1785/BSSA0870041078.
- Martin, E. R. *Passive Imaging and Characterization of the Subsurface with Distributed Acoustic Sensing*. PhD thesis, Thesis, Dept. of Geophysics, Stanford University, Stanford, CA, 2018. 443, 2018.
- Mata Flores, D., Sladen, A., Ampuero, J.-P., Mercerat, E. D., and Rivet, D. Monitoring Deep Sea Currents with Seafloor Distributed Acoustic Sensing. Oct. 2022. doi: 10.1002/es-soar.10512729.1.
- Mateeva, A., Mestayer, J., Cox, B., Kiyashchenko, D., Wills, P., Lopez, J., Grandi, S., Hornman, K., Lumens, P., Franzen, A., Hill, D., and

- Roy, J. Advances in Distributed Acoustic Sensing (DAS) for VSP. In *SEG Technical Program Expanded Abstracts 2012*, SEG Technical Program Expanded Abstracts, pages 1–5. Society of Exploration Geophysicists, Sept. 2012. doi: 10.1190/segam2012-0739.1.
- Mateeva, A., Lopez, J., Potters, H., Mestayer, J., Cox, B., Kiyashchenko, D., Wills, P., Grandi, S., Hornman, K., Kuvshinov, B., Berlang, W., Yang, Z., and Detomo, R. Distributed Acoustic Sensing for Reservoir Monitoring with Vertical Seismic Profiling: Distributed Acoustic Sensing (DAS) for Reservoir Monitoring with VSP. *Geophysical Prospecting*, 62(4):679–692, July 2014. doi: 10.1111/1365-2478.12116.
- Mizuno, K., Cristini, P., Komatitsch, D., and Capdeville, Y. Numerical and Experimental Study of Wave Propagation in Water-Saturated Granular Media Using Effective Method Theories and a Full-Wave Numerical Simulation. *IEEE Journal of Oceanic Engineering*, 45(3):772–785, 2020. doi: 10.1109/JOE.2020.2983865.
- Muir, J. B. and Zhan, Z. Wavefield-based evaluation of DAS instrument response and array design. *Geophysical Journal International*, 229(1):21–34, 2022. doi: 10.1093/gji/ggab439.
- Nakazawa, M. Rayleigh Backscattering Theory for Single-Mode Optical Fibers. *JOSA*, 73(9):1175–1180, Sept. 1983. doi: 10.1364/JOSA.73.001175.
- Ogden, H. M., Murray, M. J., Murray, J. B., Kirkendall, C., and Redding, B. Frequency Multiplexed Coherent φ -OTDR. *Scientific Reports*, 11(1):17921, Sept. 2021. doi: 10.1038/s41598-021-97647-z.
- Papp, B., Donno, D., Martin, J. E., and Hartog, A. H. A Study of the Geophysical Response of Distributed Fibre Optic Acoustic Sensors through Laboratory-Scale Experiments: Geophysical Response of Fibre Optic Sensors. *Geophysical Prospecting*, 65(5): 1186–1204, 2016. doi: 10.1111/1365-2478.12471.
- Rivet, D., de Cacqueray, B., Sladen, A., Roques, A., and Calbris, G. Preliminary Assessment of Ship Detection and Trajectory Evaluation Using Distributed Acoustic Sensing on an Optical Fiber Telecom Cable. *The Journal of the Acoustical Society of America*, 149(4):2615–2627, 2021. doi: 10.1121/10.0004129.
- Sanchez-Palencia, E. *Non homogeneous media and vibration theory*. Number 127 in Lecture Notes in Physics. Springer, Berlin, 1980.
- Singh, S., Capdeville, Y., and Igel, H. Correcting wavefield gradients for the effects of local small-scale heterogeneities. *Geophysical Journal International*, 220(2):996–1011, 2020. doi: 10.1093/gji/ggz479.
- Sladen, A., Rivet, D., Ampuero, J.-P., De Barros, L., Hello, Y., Calbris, G., and Lamare, P. Distributed Sensing of Earthquakes and Ocean-Solid Earth Interactions on Seafloor Telecom Cables. *Nature communications*, 10(1):1–8, 2019. doi: 10.1038/s41467-019-13793-z.
- van den Ende, M., Ferrari, A., Sladen, A., and Richard, C. Next-Generation Traffic Monitoring with Distributed Acoustic Sensing Arrays and Optimum Array Processing. In *2021 55th Asilomar Conference on Signals, Systems, and Computers*, pages 1104–1108. IEEE, 2021.
- van Driel, M., Wassermann, J., Nader, M. F., Schuberth, B. S. A., and Igel, H. Strain Rotation Coupling and Its Implications on the Measurement of Rotational Ground Motions. *Journal of Seismology*, 16(4):657–668, Oct. 2012. doi: 10.1007/s10950-012-9296-5.
- Wang, B., Mao, Y., Ashry, I., Al-Fehaid, Y., Al-Shawaf, A., Ng, T. K., Yu, C., and Ooi, B. S. Towards Detecting Red Palm Weevil Using Machine Learning and Fiber Optic Distributed Acoustic Sensing. *Sensors*, 21(5):1592, Jan. 2021. doi: 10.3390/s21051592.
- Wang, H. F., Zeng, X., Miller, D. E., Fratta, D., Feigl, K. L., Thurber, C. H., and Mellors, R. J. Ground Motion Response to an ML 4.3

Earthquake Using Co-Located Distributed Acoustic Sensing and Seismometer Arrays. *Geophysical Journal International*, 213(3): 2020–2036, June 2018. doi: 10.1093/gji/ggy102.

- Williams, E. F., Fernández-Ruiz, M. R., Magalhaes, R., Vanthillo, R., Zhan, Z., González-Herráez, M., and Martins, H. F. Distributed Sensing of Microseisms and Telesseisms with Submarine Dark Fibers. *Nature Communications*, 10(1):5778, Dec. 2019. doi: 10.1038/s41467-019-13262-7.

A Discrete differentiation along cables and homogenization

The following development is similar to that in Singh et al. (2020), appendix B. In Sec. 5.2, we have assumed that a DAS is measuring the strain along the FO whereas they are measuring

$$\Delta_x u_x(\mathbf{x}, t) = \frac{u_x(\mathbf{x} + L_G \hat{\mathbf{x}}, t) - u_x(\mathbf{x}, t)}{L_G}, \quad (22)$$

where, for the sake of simplicity, we have assumed once again that the cable is parallel to the x -axis. For smooth spatial variations of u_x , $\Delta_x u_x$ is a good approximation of $\partial_x u_x$. Nevertheless, as we have seen earlier, in the presence of localized heterogeneities near the cable, u_x is only smooth at the leading order of the homogenization series, and not at the first order.

In the following, we use a Cartesian coordinate system for the microscopic-scale domain (for the \mathbf{y} vector) in which $\hat{\mathbf{y}}_x$ and $\hat{\mathbf{y}}_z$ are the horizontal and vertical unit vectors, respectively. We start from the order 1 expression of the x -component of the effective velocity:

$$u_x(\mathbf{x}, t) = u_x^*(\mathbf{x}, t) + \varepsilon \chi_{xij}(\mathbf{x}, \mathbf{y}) \epsilon_{ij}^*(\mathbf{x}, t) + O(\varepsilon^2). \quad (23)$$

Because variations along \mathbf{x} are smooth and variations along \mathbf{y} are not, we can use a first-order Taylor expansion only along x :

$$u_x^*(\mathbf{x} + L_G \hat{\mathbf{x}}, t) = u_x^*(\mathbf{x}, t) + L_G \partial_x u_x^*(\mathbf{x}, t) + O(L_G), \quad (24)$$

$$\epsilon^*(\mathbf{x} + L_G \hat{\mathbf{x}}, t) = \epsilon^*(\mathbf{x}, t) + L_G \partial_x \epsilon^*(\mathbf{x}, t) + O(L_G), \quad (25)$$

$$\begin{aligned} \chi(\mathbf{x} + L_G \hat{\mathbf{x}}, \mathbf{y} + \frac{L_G}{\varepsilon} \hat{\mathbf{y}}_x) &= \chi(\mathbf{x}, \mathbf{y} + \frac{L_G}{\varepsilon} \hat{\mathbf{y}}_x) \\ &+ L_G \partial_x \chi(\mathbf{x}, \mathbf{y} + \frac{L_G}{\varepsilon} \hat{\mathbf{y}}_x) \\ &+ O(L_G). \end{aligned} \quad (26)$$

Combining the five equations above and truncating to the leading order both in ε and L_G , we find

$$\Delta_x u_x(x, t) = \partial_x u_x^*(\mathbf{x}, t) + \tilde{\Xi}_{xij} \epsilon_{ij}^*(\mathbf{x}, t) + O(\varepsilon, L_G), \quad (27)$$

where

$$\tilde{\Xi}_{ijkl} = \text{Sym}_{ij} \left(\frac{\chi_{jkl}(\mathbf{x}, \mathbf{y} + \delta y \hat{\mathbf{y}}_i) - \chi_{jkl}(\mathbf{x}, \mathbf{y})}{L_{Gy}} \right), \quad (28)$$

$L_{Gy} = \frac{L_G}{\varepsilon}$ and Sym_{ij} is the symmetric tensor with respect to the i, j indexes.

If χ variations along \mathbf{y} are oscillating at a smoother pace than $2L_G/\varepsilon$, then $\Xi \simeq \tilde{\Xi}$ and eq. (27) equal eq. (20).

Nevertheless, in general, there is no reason for the χ variations to be smooth implying that the L_G/ε sampling along y_x can lead to aliasing. In general, Ξ and $\tilde{\Xi}$ are therefore different. Nonetheless, using $\tilde{\Xi}$ instead of Ξ in eq. (20) doesn't change the point of the paper. It only changes the interpretation one can make of the measurement obtained from a DAS system. Indeed, without any hypothesis on the regularity of Ξ , using $\tilde{\Xi}$ to infer something about the underlying mechanical properties promises to be difficult.

The article *DAS sensitivity to heterogeneity scales much smaller than the minimum wavelength* © 2024 by Yann Capdeville is licensed under CC BY 4.0.